33RD CONGRESS
OF THE INTERNATIONAL COUNCIL
OF THE AERONAUTICAL SCIENCES
STOCKHOLM, SWEDEN, 4-9 SEPTEMBER, 2022

ICAS 2022 SWEDEN

VALIDATION STUDY OF BLUNTED AND SHARP CONES AT HYPERSONIC SPEED

Einar Karl T. Carias[1] & Simon A. Prince[1]

[1]School of Aerospace, Transport and Manufacturing, Cranfield, Bedfordshire, MK43 0AL, UK

Abstract

The circular cone shaped nose has been the prime interest of study for high speed aerodynamics for quite some time. It is the fundamental shape which most general forebody designs are derived from. Besides from its simplicity, the flow field it produces can be easily studied since the flow is conical in nature. This study aims at investigating blunted and sharp cones in the hypersonic flow regime. The results showed Navier-stokes CFD to be effective tool for investigating hypersonic flow at low to moderate angles of attack. At higher angles of attack, above about 8 degrees, the flow separations that result from the leeside adverse pressure gradients, result in complex 3D flows that belay the underlying geometric simplicity, which are sensitive to turbulence modelling and can prove difficult for CFD to predict. Comparisons of heat transfer data, revealed the superior accuracy using an equilibrium real gas model compared with the perfect gas model.

Keywords: Computational Fluid Dynamics(CFD), Hypersonic flow, Missile forebodies.

1. Introduction

Roughly 70 years ago Chuck Yeager surpassed Mach 1 in the experimental Bell-X1 aircraft. Since then aircraft have flown at ever increasing Mach number, necessitating the investigation of the physical effects that high temperatures and very low densities have on the air which do not exist in purely low supersonic flows. These 'real gas' effects were found to significantly change the flow characteristics and therefore the forces and heating characteristics in what is now called 'hypersonic' flow. The space sector, in particular, drove the developing understanding of hypersonic aerodynamics, but is of renewed interest in the military application of hypersonic missiles.

Hypersonic flows are characterised by the presence of very thin shock layers, as well as the rapid growth of the boundary layer. At hypersonic speed the boundary layer thickness growth $\propto M_{\infty}^{2}$, and so the displacement effects of the boundary layer strongly affect the location and strength of the shock wave in a way not seen in purely supersonic flow.

A more dominant aspect of hypersonic flow is the high temperature that arises in the shock layer, along with the substantial frictional heating in the boundary layers. In the hypersonic regime, the flow cannot be assumed to be calorifically perfect ($\gamma = 1.4$), since some of the internal energy of the gas will go into vibrating the atoms in the gas molecules, and not all of it into the thermal translational and rotational energy modes. At extreme temperatures the energy may also be enough to break the molecules and initiate chemical reactions, and ultimately to ionize the free atoms to form a plasma. A real gas model, such as that by Gupta et al. [14] must then be used to calculate the thermo-chemical equilibrium state. The computational fluid dynamics (CFD) codes used to model or simulate low speed flows, assuming perfect gas and constant γ, must then be considerably extended to include the modelling of these real gas effects.

A common forebody geometry seen in most hypersonic vehicle and weapon designs is the blunted cone, which has the benefit of relatively low drag and low heat transfer characteristics. Despite its simplicity, however, the flow field generated around it in hypersonic flight at moderate to high angle of attack can be quite complex, involving smooth surface boundary layer separation, the formation of leeside vortices and complex embedded secondary shock waves. This paper, therefore aims to assess whether a modern commercial Navier-Stokes CFD code, namely the STAR-CCM+ solver, as used in a similar study by Cross and West [7], with and without real gas modelling, can accurately predict the complex 3D viscous hypersonic flows around conical forebodies.

2. Hypersonic Flows around Sharp and Blunted Cones.

At zero angle of attack the hypersonic flow past a sharp cone is very simple, involving an attached conical shock wave and the growth of an attached boundary layer on the cone surface, which may be laminar, turbulent or transitional. Apply an angle of attack and the flowfield develops increasing complexity. The shock layer on the windward side reduces in thickness, and a crossflow develops around the cone resulting in non-constant surface pressure distribution. The surface pressure on the leeside of the body becomes adverse and the leeside boundary layer will tend to separate, forming a shear layer that can roll up to form a leeside vortex system, as shown in Figure 1a. Depending on the Mach number and angle of attack combination, secondary internal shock waves can form associated with the displacement effect of the separated flow / vortices. Rainbird [28] stated that such flowfields can be defined as essentially conical and symmetrical even with the presence of separation. The study by Bannink and Nebbeling [2] presented an oil flow visualisation shown in Figure 1b. These results were taken at Mach 2.94 at incidence angle $18°$. The internal shock wave is present due to the flow mach number reaching supersonic while it is accelerating from the windward to the leeward meridian. This causes boundary layer separation, which induces the primary and secondary vortex structure.

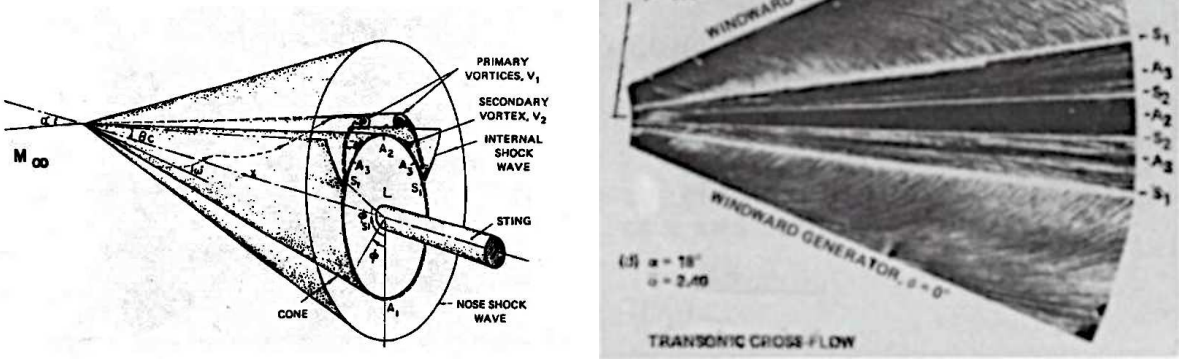

(a) Sketch of the vortex structure at high angles of attack

(b) Oil flow visualisation of the skin friction lines over the cone

Figure 1 – Shockwave and symmetric vortex structure on a cone at high angles of attack [30]

The effect of blunting the nose of the cone has been studied by many researchers. This leads to a detached bow shock wave and the imposition of a strong adverse axial pressure gradient on the nose which can lead to flow separations. For instance, a local Werle-Legendre [44, 19] type boundary layer separation could occur, as shown in Figure 2. Here, the resulting shear layer is focused into a spiral vortex emanating tangentially from the surface before merging into the primary vortices formed further

downstream as shown in Figure 1. Although the study by both Werle and Legendre are for low speed flow, their interpretation for the singularities in skin friction pattern close to the point of separation is still valid at high speeds [27]. In this region of separation, high heating rates are also observed at increasing angles of incidence. In the experiment of Zakkay et al. [45] on a $10°$ blunt cone at Mach 6 with incidence angle $20°$ shown in Figure 2c the oil flow photographs clearly showed the separate streamwise separations from the nose and crossflow separations further aft.

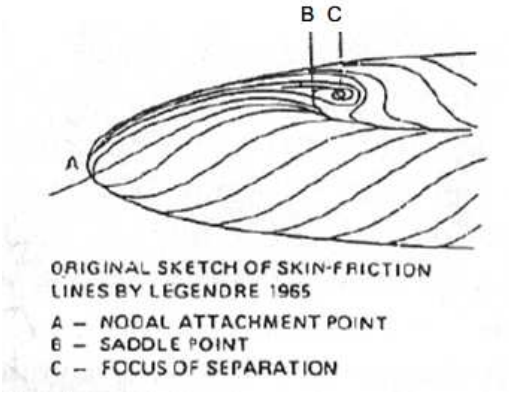

(a) Sketch of skin-friction lines for blunted noses

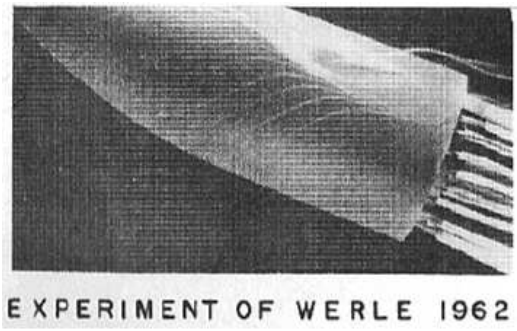

(b) Oil flow visualisation of the skin friction lines over a blunted cone

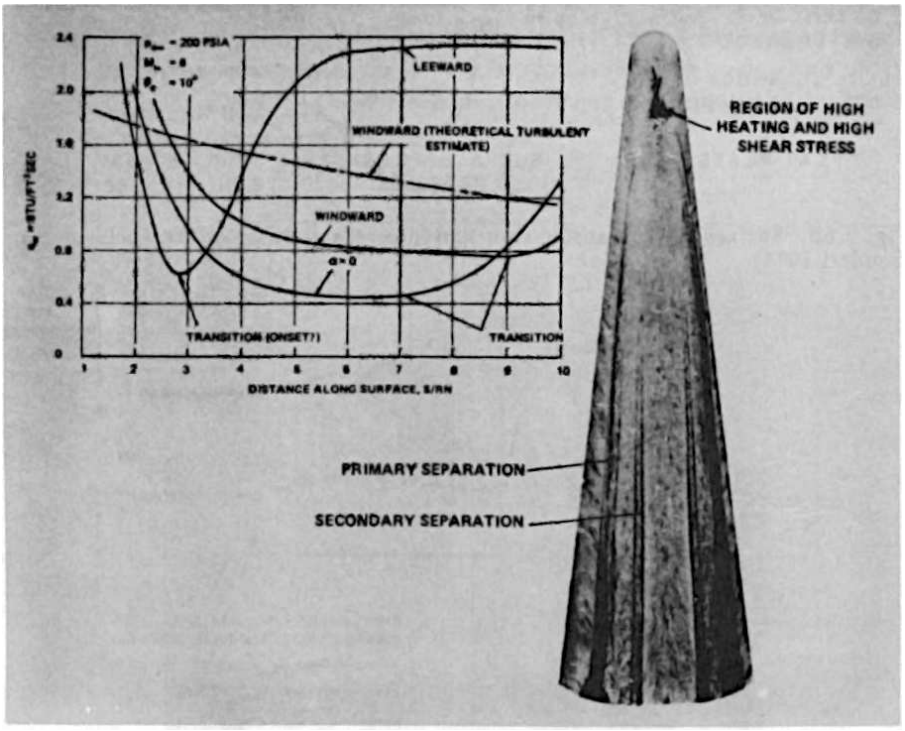

(c) Zakkay et al. [45] Experiment Heat transfer rates and Oil flow

Figure 2 – Vortex structure for blunted noses [30]

2.1 Theoretical Prediction Methods for Sharp Cones

One of the first theoretical methods for the prediction of the inviscid 3D flow around a sharp nosed cone at supersonic and hypersonic speeds was that by Taylor and Maccoll. Further methods for more generalised 3D supersonic flows used linearised theory included references [41, 20, 38, 15, 3]. These provide good design estimates of the aerodynamic forces and are also in good agreement with the experiments.

For the hypersonic flow regime, Van Dyke [39] developed a theory that permitted an analytical solution

which also linearizes the Taylor Maccoll equation. This was possible due to a "constant-density approximation" in the hypersonic flow regime. It allows for a solution with remarkable accuracy at high mach number and small cone angles. Later this theory was applied to the unyawed cone by Rasmussen [29].

The exact zero angle of attack solutions were improved upon by Stone [36] to obtain valid results for small angle of attack cases. These works were developed further by Kopal [16] and Sims [32]. However, Stone's straight-forward perturbation theory contradicts the energy equation for steady inviscid adiabatic flow, which identifies entropy to be constant on a streamline, and thus must be constant on the cone's surface. A study by Ferri [11] pointed out that every streamline crossing the shockwave, assumed to be attached to the inclined cone, must curve around it and reach the top generator of the cone. The entropy jump across the shockwave varies from streamline to streamline due to the curvature of the shockwave. Ferri called the top generator region the vortical singularity region. This region at high angle of attack could detach from the surface of the cone. The thin layer of intense vorticity near the cone surface is referred as the vortical layer by Ferri.

The very first theoretical model of fluid flow can be applied to hypersonic flows, where its validity is most appropriate. Isacc Newton developed his corpuscular theory of fluid flow, whereby the flow is composed of a stream of individual non-interacting molecules or particles, all travelling in one direction. When the stream of particles hits a surface, Newton postulated that the normal component of momentum of the fluid is assumed to disperse, while the tangential component is conserved. This is called the Newtonian Impact theory, which predicts that the surface pressure coefficient on such a surface, $C_p = 2sin^2\theta$, where θ is the flow deflection and the 2 term represents the stagnation Cp. This model, as well as the modified version ($C_p = C_{p_{stag}} sin^2\theta$, where stagnation point pressure is more accurately calculated manually), allows for a quick engineering estimate of the aerodynamic forces of simple shapes.

Referring back to the vortical layer, one of the earliest studies was carried by Cheng [5]. Using Newtonian Impact theory, Cheng found an approximate analytical solution to Stone's problem. Without being restricted to the Newtonian theory, Cheng thereafter used the modified expansion scheme to investigate the near surface flows of the cone. The results were uniformly valid to first order with angle of attack. Doty and Rasmussen [10] derived an analytical solution to Stone's problem, much like Cheng, but without the constraints of the Newtonian approximation. Their approximate theory provide an accurate analytical interpretation of the outer flow over an inclined cone in hypersonic flow.

More recently high fidelity CFD, via the solution of the Navier-Stokes equations, have allowed viscous effects and surface heat transfer to be predicted along with surface pressures. These have been augmented with real gas models to predict the vibrational energy modes and chemical equilibrium based on the local temperature. While this has been found adequate for many hypersonic flows, those with intense heat-transfer rates have proved difficult to match with experimental results. An example of this was the study of turbulent flow with a perfect-gas fluid property at Mach 9 [9]. Four different solutions were found for the heat transfer due to the ambiguity with mesh generation and turbulence modelling.

2.2 Bluntness effects

As previously discussed, hypersonic reentry vehicles experience very high surface heating. An attached shock wave on a sharp tipped cone with high temperature supersonic flow behind will retain very high frictional heating at the nose, which can cause melting and structural damage. Blunting the nose produces a detached shock wave and low subsonic flow around the nose that drastically reduces frictional heating through the boundary layer, despite higher shock layer temperatures.

Ambrosio and Wortman [1] and Billig [4] found an empirical relation for the detachment distance and shock wave shape for blunted bodies, as a function of freestream Mach number, nose radius and cone radius. They also found that a heavily rounded nose leads to considerably higher drag. On the other hand, small bluntness ratio noses has shown significant benefits, including reduction of total heat transfer due to the reduction of surface skin friction.

Ward [43] investigated 16 nose models, with varying shape to investigate drag reduction with nose blunting at Mach 3. Ward's results have shown that the amount of nose blunting required to achieve minimum drag reduces as forebody fineness ratio (the ratio between the body's length to its diameter) is increased. Drag results for forebody fineness ratio less than 0.6 of truncated and spherically-bunted cones are noticeably less than a sharp cone of similar fineness ratio. Ward also emphasized that a blunted nose resulted in a lower peak heat transfer rate to the body.

At higher Mach ranges (Mach 1.2-7.4), Sommer and Stark [34] found that drag penalties of blunted noses exponentially increase at increasing Mach numbers. However at lower Mach numbers of 1.5 and below, these penalties were mitigated using a larger blunting ($\approx$ 0.5 and up) of the nose. Similarly, Wallskog and Hart [42] concluded identical findings in their investigation. They tested fin-stabilised slender bodies with spherical, flat and conical noses at Mach 0.6-2.3. Their experiment involved launching the blunted nose models from the ground and accelerated using a two-stage propulsion system. Drag data were collected in coasting flight for each model. Again, small degrees of blunting did not contribute to the increase drag up to Mach 1.1. But over the entire supersonic range of the test, a buildup of drag was witnessed as bluntness was increased with increasing Mach number. Small degrees of bluntness gave a maximum 4% of drag reduction compared to no blunting at all.

At the beginning of the 21st century, The HyShot flight experiment [26] was developed to compare wind tunnel data with free flight experiment. Deepak et al. [8] utilised the results from the HyShot program to correlate a nose-cone shape optimisation code. The optimisation tool used a PARSEC curve approach [33] for obtaining the optimised nose cone design. Using CFD, this approach of blunting the nose cone gave a significant drag reduction (7% at Mach 3 and 10% in Mach 8).

3. Numerical Analysis Method

Computational Fluid Dynamics takes advantage of the mathematical solution of the governing flow equations in order predict the flow properties around bodies with a given set of initial conditions via iterative processes on computers. The Navier-Stokes equations are the full governing equations describing continuum, viscous, unsteady compressible flows, most often solved with domains discretised into cells via Gauss divergence theorem as a part of Finite Volume Method, where the conservation of mass, momentum and energy is conserved with each cell. [40]. This study employed the STAR-CCM+ commercial flow solver which features real gas models for the solution of hypersonic flows. The solver was used to assess the ability of modern CFD methods to predict the flows about three cone models, each having experimental data for comparison.

3.1 The Geometries

The three experimental studies used for CFD assessment were by Tracey [37] (sharp cone) and Cleary [6] (blunted cones). The sharp cone, with a $10°$ semi-apex circular cone, test cases were simulated at Mach 7.9 at an angle of attack of $4°$ to $24°$ in $4°$ increments. The two blunt nosed models were simulated at Mach 5, 7 and 10 at angles of attack (AoA) $0°$, $2°$, $5°$, $10°$ and $15°$. Both models have a blunting radius of 1 inch but differ in half cone angle, one having $15°$ and the other a slightly larger $30°$ but with shorter length.

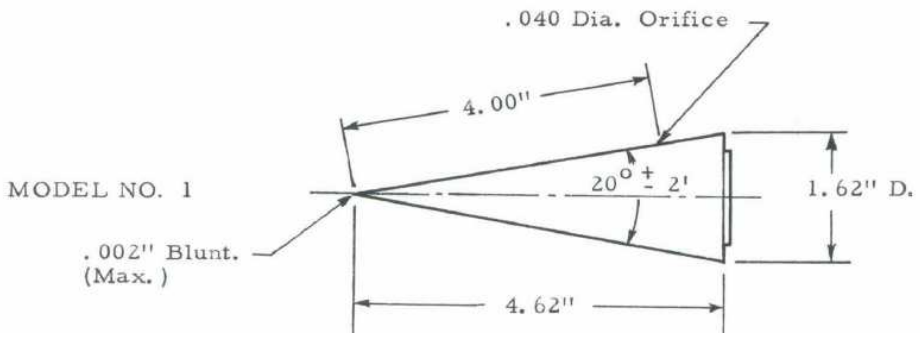

(a) Sharp cone model dimensions in inches Tracey [37]

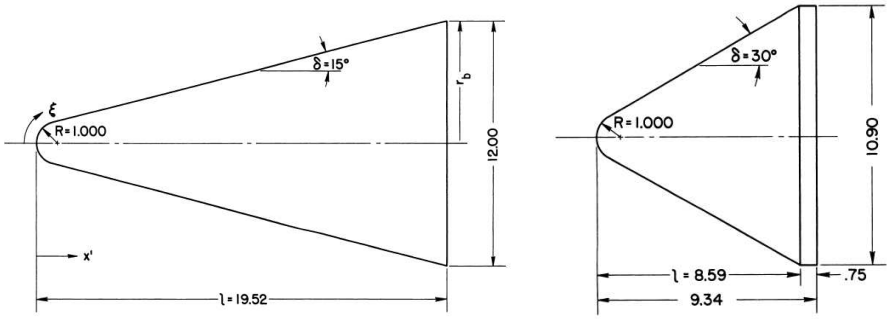

(b) Blunted cone models dimensions in inches Cleary [6]

Figure 3 – Sharp and blunted cone models

3.2 Grid Generation

For all three test cases a C-type topology was chosen for the flow domain in order to capture both attached and detached shock waves. Half of the flow was modelled, with a symmetry boundary condition applied since the experimental flows were shown to be symmetric about the plane linking the windward attachment and leeward separation lines. The fluid domains for each case are presented in Figure 4. Far field, outlet and symmetry domain employed the free-stream (orange surfaces), pressure outlet (brown), and symmetry (blue) boundary conditions, respectively. The Tracey cone model featured a sting/afterbody, but the sting mounting the blunted models was not modelled, as the base flow was not expected to affect the flow on the cone itself.

The far extent of the domain was determined by the generated shock wave at the highest AoA of the test. An estimate of the shock angle at zero AoA was calculated using the Taylor-Maccoll [21] equation and was then extended to further accommodate at the highest corresponding AoA. Using flat plate boundary layer theory [31], the first cell height was calculated to ensure the viscous sub layer was properly captured with a Y+ value of 1 near the nose.

A structured mesh was generated using Fluent ICEM for the sharp cone case, given by its simplicity. Having a structured mesh provided several advantages mainly its computing efficiency, since the cells are more aligned with the flow. From the mesh sensitivity analysis, detailed in section 3.4, the intermediate sized mesh was selected and is shown in Figure 5.

The quality of the mesh was assessed using two criteria, angle and determinant (2x2x2), and smoothing performed to ensure 99% of the cells has a determinant greater than 0.4 and angle of at least $18°$.

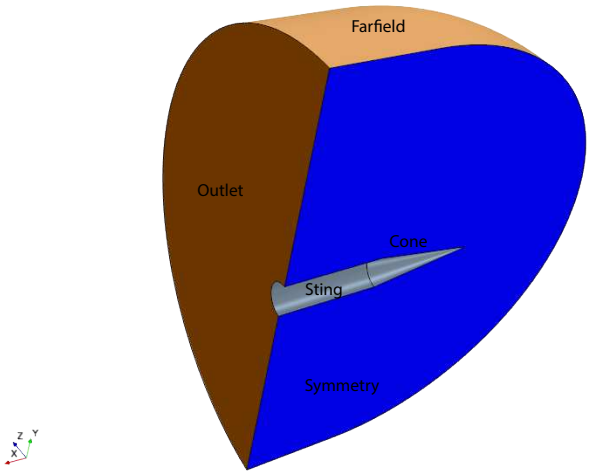

(a) Sharp cone model

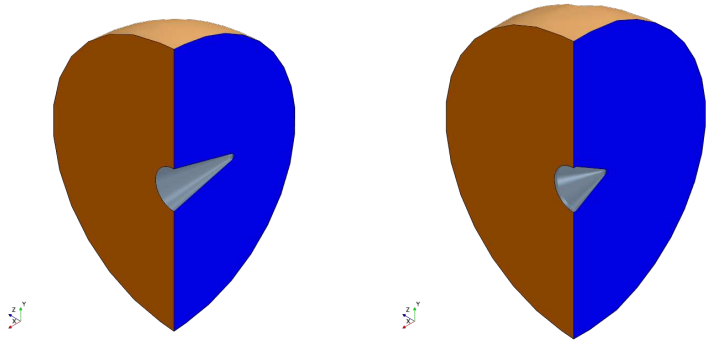

(b) Blunted cone models

Figure 4 – Fluid Domains for the three cases

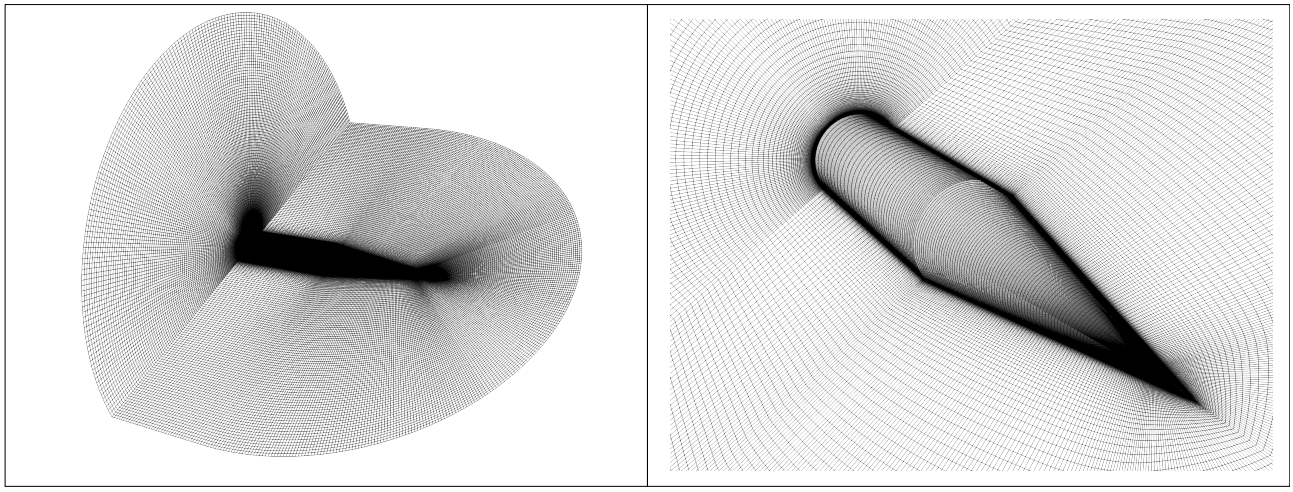

Figure 5 – Generated sharp cone mesh (hidden far field)

The mesh for the blunted cone was generated using STAR-CCM+ meshing to generate unstructured hybrid meshes, which are globally unstructured but with prismatic layers to solve the viscous sub-layer. More information about the hybrid mesh merits over structured mesh could be found in the literature [22, 23].

Figure 6 presents the blunted cone meshes. Instead of a conventional tetrahedral unstructured mesh, a polyhedral mesh was utilised. Polyhedral meshes are relatively efficient and easy to build, but generally contain approximately five times fewer cells for a given starting surface than tetrahedral cells. A special dualization scheme was used to create the polyhedral cells from an underlying tetrahedral equivalent, which is automatically created as part of the process. The process is explained more in detail in [12, 13].

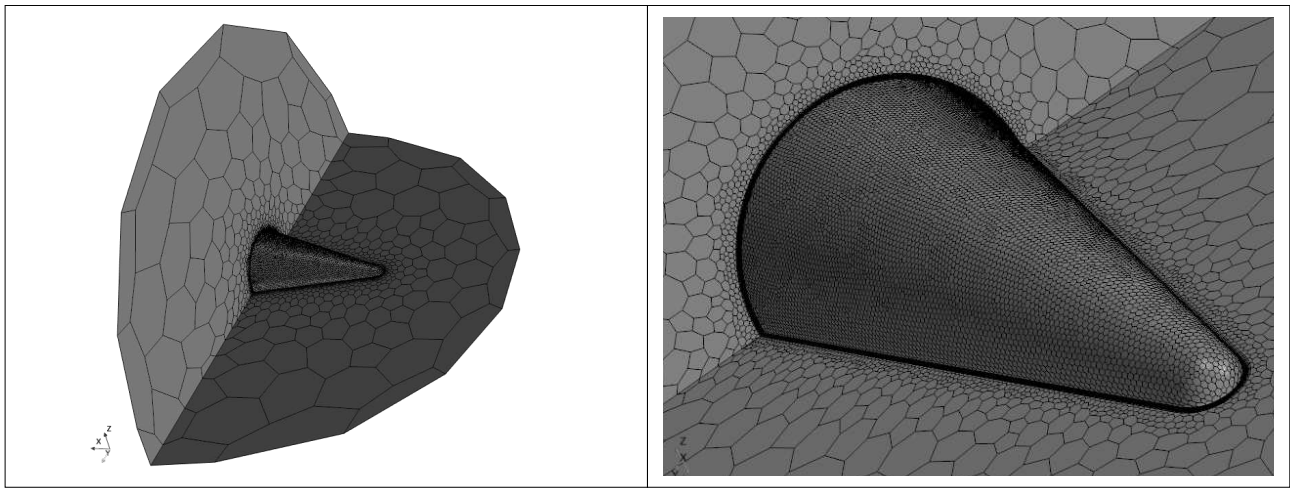

(a) 15°

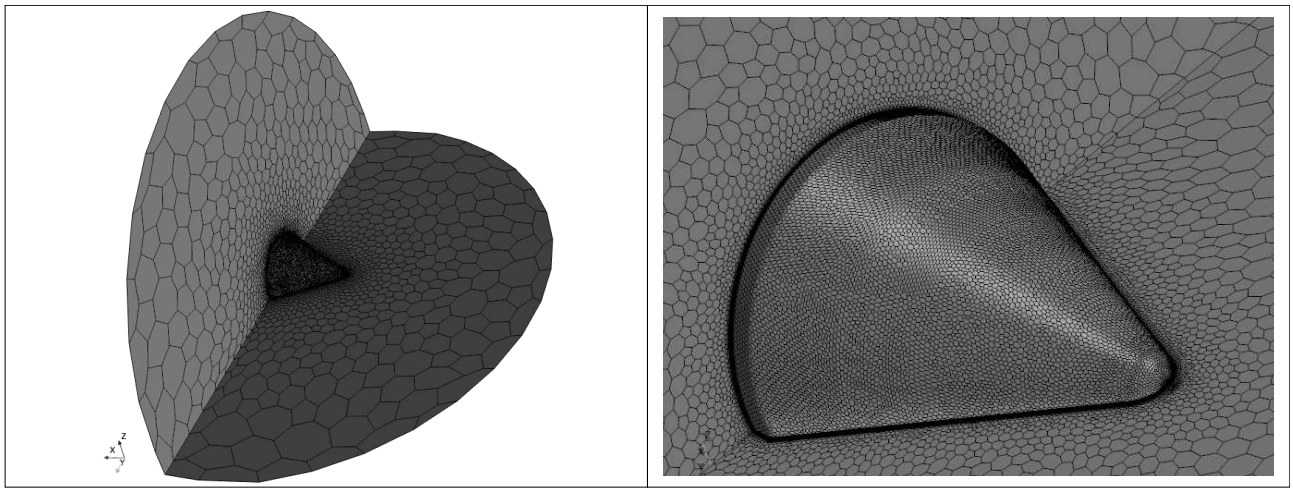

(b) 30°

Figure 6 – Generated blunted cone mesh (hidden far field)

3.3 Simulation Parameters

3.3.1 Gas Model

The most important reason of choosing STAR-CCM+ for the test cases is that it has Real Gas air property models encoded. The equilibrium gas and ideal gas was chosen as the gas model for the simulations, to assess the influence of the real-gas effects. In this case the Gupta et al[14] equilibrium gas model was used. This model considers the effects of internal energy excitation, molecular dissociation and associated chemical reactions. However, it is important to note that this model's key assumption is that the gas is thermochemically in equilibrium, i.e. the timescales it takes to complete these physical processes are very fast relative to the flow timescale. Furthermore, this model is valid up to 30,000K temperature and pressures between 0.0001 to 100 atmospheres. When this model is selected, the properties of the material [1] are calculated as the function of temperature and pressure.

[1] Material properties consists of: viscosity, specific heat, thermal conductivity, and speed of sound.

3.3.2 Boundary Conditions

The Sharp Cone Case

The cone and sting surfaces were set with no-slip wall boundary conditions with no roughness effects. Tracey applied wall cooling in his experiment to maintain a temperature of 302K, and this was the isothermal condition set in the calculations. The farfield boundary was set as "freestream" boundary condition which sets a constant Mach number, static pressure and temperature. These were 7.95, 190.73 Pa and 55.38K respectively. The corresponding Reynolds number was 3.6 million based on cone generator length. Lastly, the outlet boundary was set to pressure outlet boundary condition, which fixed the outlet static pressure and temperature, which were set to the freestream values. The symmetry boundary condition enforced flow symmetry on the symmetry plane.

The Blunted Cone Cases

Similarly, the blunted cone surfaces are set with no-slip wall condition. However, no constant cooling was applied for Cleary's experiments. Hence, the thermal condition was set to adiabatic. The boundary conditions were calculated using isotropic relations for Mach 5.25, 7.4, and 10.6, the conditions being as follows:

	Mach 5.2	**Mach 7.4**	**Mach 10.6**
Pressure(Pa):	1972.59	1312.07	105.23
Temperature(K):	170.61	92.96	47.34
Re Number(million):	1.4	3.2	1.0

The same boundary condition types as the sharp cone case were applied for the pressure outlet and the symmetry plane.

3.3.3 Turbulence Models

Cross and West [7] explored all the built-in turbulence models available in Star-CCM+ applicable for hypersonic flow. Following their recommended setting, Menter-SST[24, 25] and Spalart-Allmaras[35] have been chosen as the turbulence models for the test case. In their paper, both turbulence models were found to be in reasonable agreement with the experimental results compared to the other available turbulence models within STAR-CCM+.

The settings for Spalart-Allmaras simulations were left as default. However, the Menter-SST model was slightly modified according to the recommended setting for hypersonic flows. This involved the activation of a quadratic constitutive relation, the compressibility correction deactivated and the a_1 coefficient set to 0.355.

3.3.4 Solver Settings

Steady flow was assumed for all three cases. A coupled solver was used, which solved the equations for energy, mass, and momentum flux simultaneously. For computing inviscid fluxes, the AUSM+ flux vector splitting scheme was utilised since it is proven to work well with high-speed flows[17, 18]. The MUSCL 3rd order discretization scheme provided third order spatial accuracy, with the exception in vicinity of strong shock waves [2].

STAR-CCM+ has a useful feature that automates the Courant Friedrichs Lewy (CFL) number whilst the simulation is running. This "expert driver" setting for the coupled solver automatically adjusts the CFL number to achieve a faster convergence, whilst maintaining stability. During unstable portions of the simulation, the expert driver feature reduces the CFL number and ramps back up once the difficult portions of the simulation have past. As a result, faster convergence time can be achieved compared

[2]MUSCL discretization reduced to second order spatial accuracy in vicinity of strong shocks.

to simply leaving the CFL number constant throughout. During the simulation, initial CFL number of 0.1 was set, with the maximum being 1000.

The algebraic multigrid linear solver (AMG) was used to solve the linear equations. The algebraic multigrid technique solves the differential equations in a hierarchy of meshes, instead of solving exclusively on the finest mesh. Essentially, the mesh is split into levels of coarser mesh and sequentially solved, to accelerate convergence. The turbulence solver AMG setting was kept as default but the convergence tolerance was changed to 0.001.

The continuity convergence accelerator (CCA) was also used. This solves a pressure-correction equation to accelerate the convergence of the continuity equation. Enhanced stability treatment was always enabled, as described in Cross and West's paper, as leaving this off would likely result in divergence. Moreover, leaving the under relaxation factor to the default value also results in divergence. Decreasing this to 0.01 was found to avoid trouble. However, in some test cases the CCA had to be deactivated completely for the simulation to converge.

Full details of all of the settings used are provided below:

- Positivity rate limit: 0.05
- Discretization: MUSCL third order
- Coupled inviscid flux: AUSM+
- Explicit relaxation factor: 0.75
- Expert Driver: Activated
  - Target CFL: 10
  - Initial CFL: 0.1
  - CFL ramp end iteration: 1000
  - CFL limiting target algebraic multi-grid cycle: 8
- AMG solver:
  - Convergence tolerance: 0.001
  - Cycle type: F cycle
  - Pre-sweeps: 0
  - Post-sweep: 3
  - Max levels: 2
- Grid Sequencing initialization: activated
  - CFL number: 2.5
- Continuity convergence accelerator: activated
  - Under relaxation factor: 0.01
  - Linear ramping: activated
    - Ramp end iteration: 1000 iterations
    - Under relaxation factor initial value: 0.005
  - Enhance stability treatment: activated
  - AMG solver: same as above

3.3.5 Initialisation

The STAR-CCM+ grid sequencing initialisation was utilised in this study. Within this approach, an algorithm creates a progressive refinement of meshes, from coarse mesh, only containing a few thousand cells, up to the most refined original mesh. Starting with the coarsest mesh, the inviscid solution is computed. Once a specified level of convergence is obtained, the solution is then interpolated onto the next mesh. This process is repeated until the algorithm reaches the finest mesh. With this method it is possible to obtain the initial conditions relatively quickly and provides better stability for the solver than a more traditional approach.

3.4 Grid Convergence Study

A grid convergence study was undertaken for all three test cases, the details of which are provided in this section.

The Sharp Cone Case

For the sharp cone case, the zero angle of attack case was used for the mesh sensitivity study. Here, theoretically the surface C_p is constant along the whole of the cone surface and this value was measured in the Tracey experiment. It was therefore this parameter that was used as the convergence metric.

Table 1 shows the parameters that were configured during the grid convergence study. The medium mesh was the baseline mesh generated, which is why its global parameter is 1. For this mesh, the number of cells in the axial, circumferential and radial directions was 171, 115 and 130 respectively. Coarse and Fine meshes were generated by altering the global cell multiplier parameter by a factor of 0.2, which increased or decreased the cell count on all fluid domains.

Type	Normal to wall growth ratio	Global multiplier	Number of cells
Coarse	1.2	0.8	1422798
Medium	1.2	1	2467150
Fine	1.2	1.2	3952810

Table 1 – Mesh sensitivity criteria

The results show that all three meshes predict the same value of surface C_p to five significant figures for each of the turbulence models, representing an error from the experimental value of 5.76 - 6%. The fine mesh was chosen as the definitive mesh since, although the fine mesh consists of nearly 4 million cells, the convergence time of the simulation (24 hours) was not much greater than that for the medium (22 hours). In addition, the finest mesh will also provide a better resolution when examining the flow features for the higher angle of attack cases.

Type	C_P	Experimental C_P	Error (%)
Spalart-Allmaras			
Coarse	$7.193\,412 \times 10^{-2}$	7.652×10^{-2}	5.9930
Medium	$7.193\,384 \times 10^{-2}$	7.652×10^{-2}	5.9934
Fine	$7.193\,740 \times 10^{-2}$	7.652×10^{-2}	5.9888
Menter-SST			
Coarse	$7.211\,515 \times 10^{-2}$	7.652×10^{-2}	5.7564
Medium	$7.211\,662 \times 10^{-2}$	7.652×10^{-2}	5.7545
Fine	$7.211\,749 \times 10^{-2}$	7.652×10^{-2}	5.7534

Table 2 – CFD solution compared with experimental result at zero incidence

The Blunted Cones Cases

The process for the grid convergence study of the blunted cones slightly differed from the sharp cone case. The procedure made use of mesh adaption based, in this case, on pressure gradient. This allows the solver to refine the mesh in regions of high pressure gradient (shock waves, expansions and vortex cores). The process of using STAR-CCM+ custom functions to assess the pressure gradient is well documented in Cross and West [7] paper. Essentially, the cell refinement criteria is set to 1 if the pressure differential across a cell is greater than the user-specified refinement limit, and to -1 if it is less than the coarsening limit. Otherwise, the criteria is set to zero, where the cells are left alone. The size of the cells flagged for refinement are split into smaller component cells. This prevents excessive

refinement and coarsening of the mesh. The "Normalized pressure gradient mesh refinement" version from Cross and West, was used for this study since it addresses several weaknesses of the normal pressure gradient function. Figure 7 shows 3 refinement levels for the $15°$ blunted cone case at Mach 7 with AoA $5°$. The baseline solution converged at 2000 iterations, which was then utilised as the solution for mesh adaption. It is evident that the technique emphasises the shock wave and also slightly refines the surrounding region inside the shock near the surface.

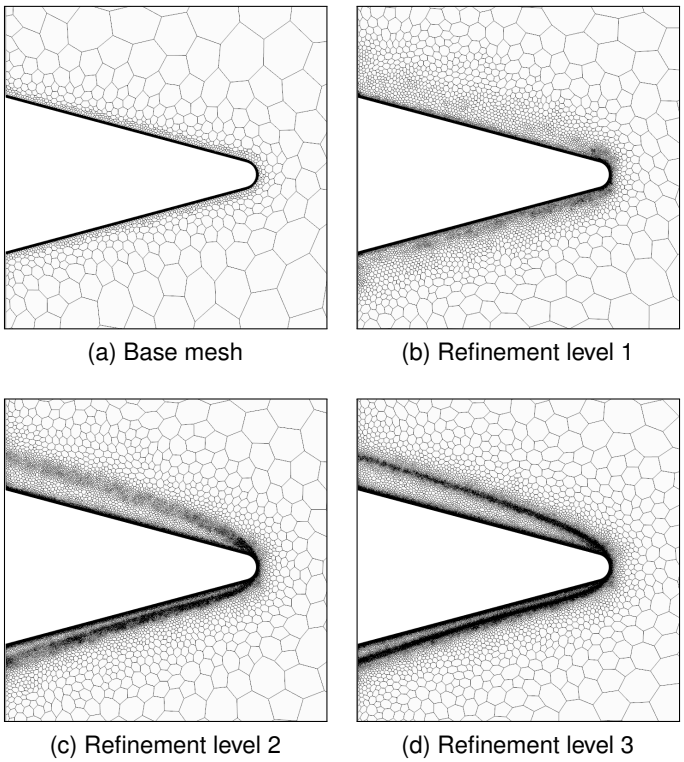

(a) Base mesh (b) Refinement level 1

(c) Refinement level 2 (d) Refinement level 3

Figure 7 – Adaptive refinement for $15°$ blunted cone at Mach 7.4, AoA $5°$

Values of lift coefficient, C_l, and drag coefficient, C_d, were the chosen criteria for each refinement level to assess mesh convergence. Looking at Figure 8, the C_d barely changes with increasing refinement level due the surface mesh at base-level being sufficiently refined. In this case, the skin-friction drag has higher contribution in total drag than wave drag. However, the value of C_l is highly dependent on the surrounding flowfield (circulation). Thus, refining the pressure gradient significantly contributes to the accuracy of the result. The mesh converged at refinement level 2 but refinement level 3 had the advantage of better resolution of the shock wave. For the rest of the study a 3 level refinement scheme was therefore adopted.

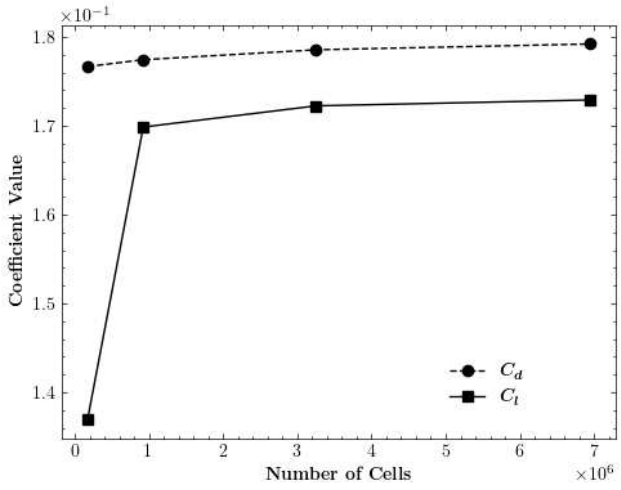

Figure 8 – C_d and C_l values at increasing cell count for refinement every 2000 iterations, M = 7.4, Spalart-Allmaras model, AoA = $10°$. .

4. Results and Discussion

The results of this project are presented in three sections: Pressure distribution, Surface heat transfer, and Flow field visualisation. The numerical results gathered from this study are compared against past experimental data from Tracey [37] and Cleary [6] papers. In Tracey's experiment, the experimental data were taken in the circumferential axis, located 4 inches longitudinally from the cone vertex. In this section, the circumferential axis will be referred to as ϕ, where ϕ=$0°$ is located at the windward meridian and ϕ=$180°$ is at the leeward meridian. In addition to surface pressure, the surface heating rates were measured and a pitot pressure traverse performed to map the crossflow structure at the same axial location. The heat transfer was measured using constantan-copper thin film heat transfer guages, while the crossflow pitot-pressure profiles were acquired using a single orifice pitot tube fixed at a particular heights above the cone surface with the model rotated about its axis to build up the pressure map Tracey [37].

The measurements on the blunted cones performed by Cleary [6] also involved the measurement of surface pressure distributions at various axial stations on the model, but also involved Schlieren photographs providing a visual description of the 3D shape of the bow shock wave which will also be used for validation.

The experimental heat transfer figures are quoted by Tracey, following detailed error analysis, to be no greater than 5%, but generally around 2% over most of the surface. The corresponding pressure measurements were quoted with an accuracy of $\pm$0.1% based on a detailed calibration of the pressure system. For the Cleary study, detailed analysis of random and systematic error in the experiment showed that a typical systematic error in determining flow Mach number of 1% caused an error of no more than 5% in pressure coefficient.

The effect of turbulence model was assessed in the study of the Tracey cone flow, as well as the effect of the real-gas model. Since these results showed, in general, the Menter-SST model provided the most accurate match with experiment, the blunt nosed cases were only computed using this turbulence model.

4.1 Surface Pressure Distribution Comparisons

The Sharp Cone Case

The results shown in Figure 9 present the circumferential C_p distributions, from the windward to the leeward meridian, comparing the experimental measurements with the corresponding modified Newtonian theory results and grid independent Navier-Stokes results with and without real gas model for the Mentor SST and Spalart-Allmaras turbulence models. At low angles of attack the distribution follows the expected cosine shape with the highest C_p along the windward attachment line, and the minimum pressure on the leeward attachment line. At higher AoA, the C_p plateaus on the leeward surface, indicating leeward side boundary layer separation. There is no peak in pressure, however, which would indicate no roll up to form a longitudinal vortex.

The agreement between all of the CFD models and experimental pressures is remarkably good, and shows that at least in surface pressure there is very little effect in turbulence model or real-gas model. Both turbulence models successfully resolved the smooth surface separation of the boundary layer.

A modified Newtonian theory prediction can also be observed in the plots. Here the C_p in the "shadow region" of the flow, post separation, was set to zero. This method is seen to underpredict the C_p magnitude on the windward side with a maximum error on the windward attachment line itself. Nonetheless, this shows how effective the Newtonian theory is for quick engineering estimates at hypersonic Mach numbers.

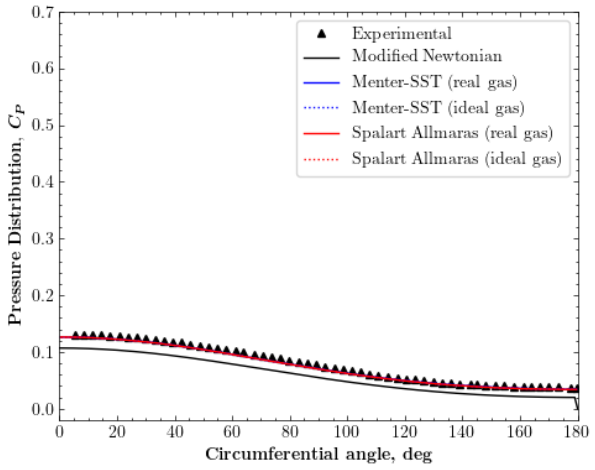

(a) AoA 4°

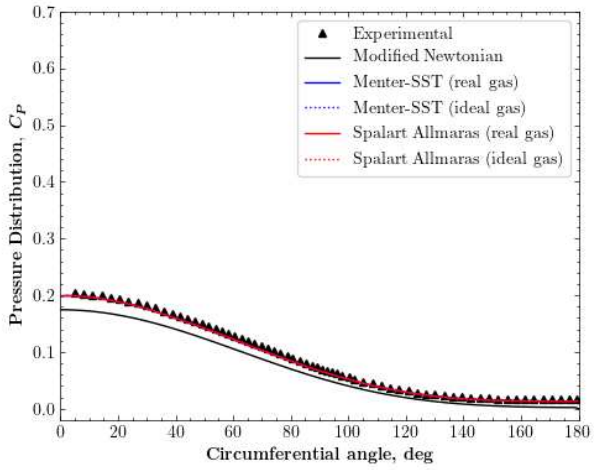

(b) AoA 8°

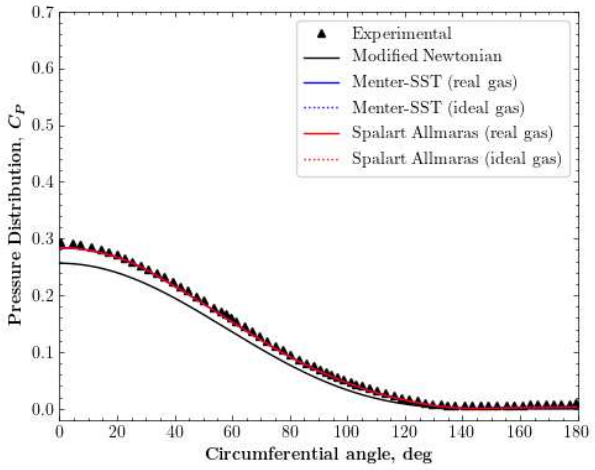

(c) AoA 12°

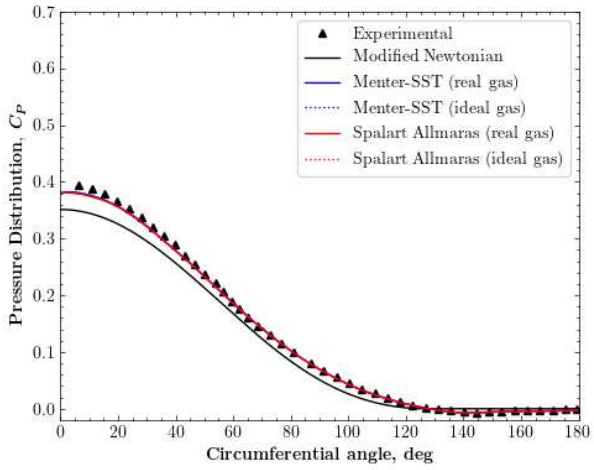

(d) AoA 16°

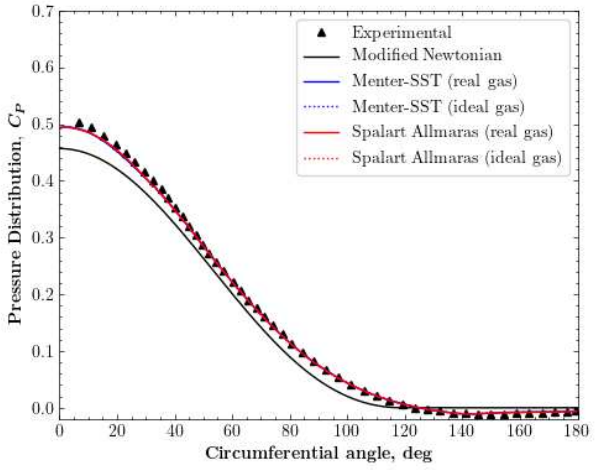

(e) AoA 20°

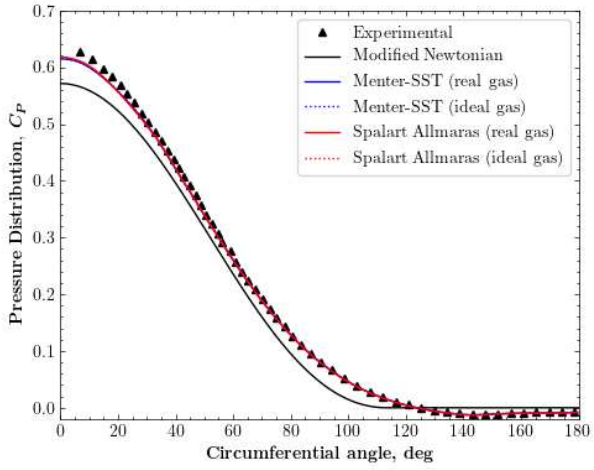

(f) AoA 24°

Figure 9 – C_p distribution of the sharp cone in the circumferential direction

The Blunted Cone Cases

The results for the blunted cone models are presented in Figure 10 - Figure 15, where the C_p distribution is plotted along the x-direction, each figure presenting comparisons of experimental and CFD (Mentor SST model and real gas model active) predicted data for different model angles of attack. Plot (a) presents these comparisons on the windward symmetry line (ϕ=0) while plot (b) presents the corresponding data on the windward symmetry line (ϕ=180) and each figure presents the comparisons for different freestream Mach number cases, M = 5.25, 7.4 and 10.6. Figure 10 - Figure 12 present the comparisons for the $15°$ half cone while Figure 13 - Figure 15 present the corresponding comparisons for the $30°$ half cone. Here the symbols represent the experimental data while the solid lines are the CFD data.

The circumferential pressure follows similar trends in the circumferential direction, but in this case the pressure varies in the x-direction. Along the windward symmetry line the pressure generally increases with angle of attack due to increased local shock strength and proximity. The flow stagnates at the nose apex and then accelerates around the rounded nose, before recovering over the conical afterbody. The corresponding flow around the leeward symmetry involves a very rapid acceleration from the stagnation point to a recovery at much lower pressure than seen on the windward symmetry line.

The experimental results of Cleary present a degree of experimental scatter, with an error of less than $\pm$5%. Nonetheless, the effects of AoA and ϕ are consistent for all mach numbers. The agreement between experimentally measured and the CFD computed results are generally very good, given the higher level of experimental uncertainty in this data compared with that of the Tracey experiment. The CFD data accurately captures all of the correct trends with the best agreement seen for the $15°$ model.

These results clearly demonstrate the capability of modern Navier-Stokes CFD methods, with real-gas models to capture the energy used in vibrating molecules, and dissociation and chemical reactions occuring in certain areas of the flow (in this case in the shock layer close to the nose), and an appropriate turbulence model, to accurately predict surface pressure distributions on hypersonic bodies from low to moderate angles of attack.

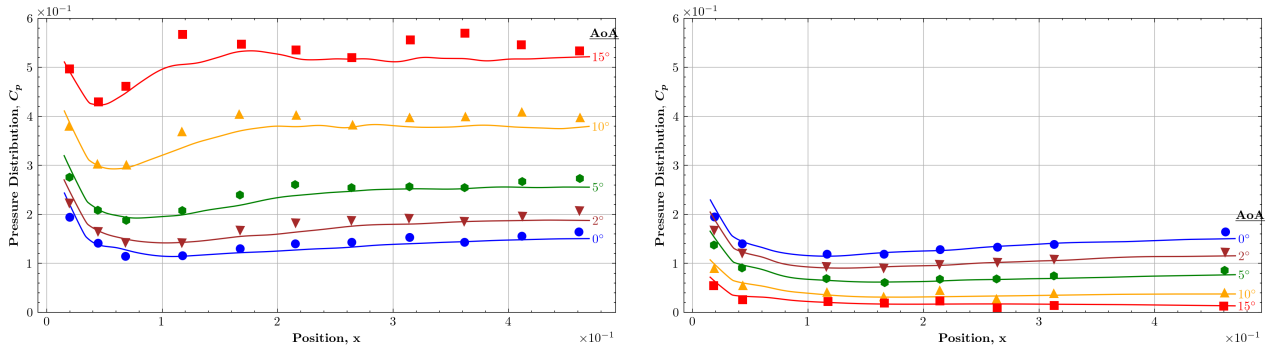

(a) ϕ 0° (b) ϕ 180°

Figure 10 – Model 1 ($15°$ half cone) C_p distribution along the x-axis at Mach 5.25

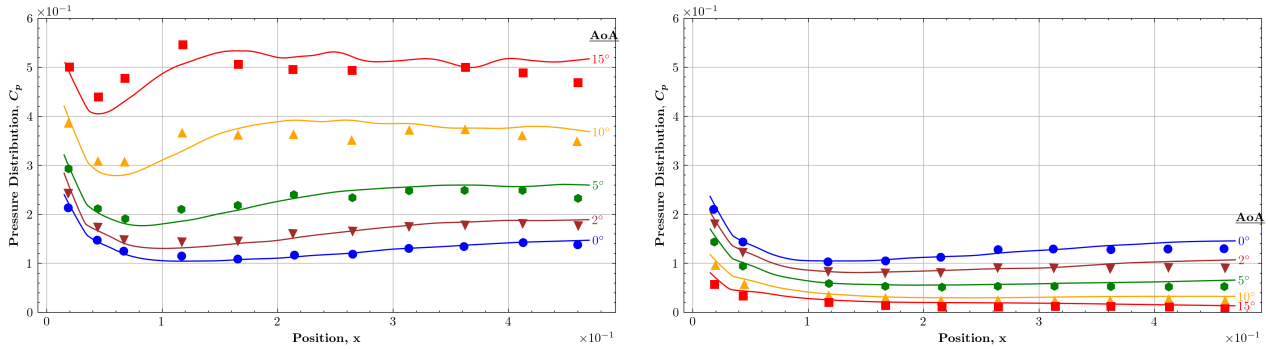

(a) ϕ 0° (b) ϕ 180°

Figure 11 – Model 1 (15° half cone) C_p distribution along the x-axis at Mach 7.4

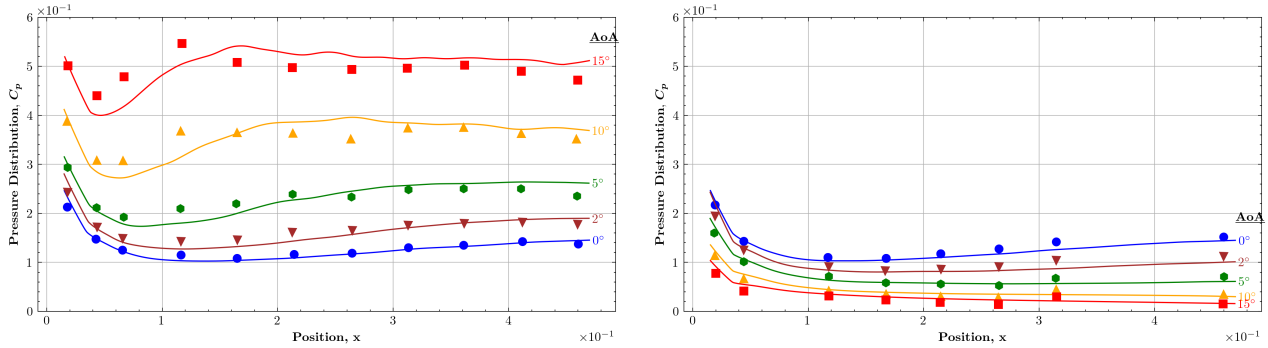

(a) ϕ 0° (b) ϕ 180°

Figure 12 – Model 1 (15° half cone) C_p distribution along the x-axis at Mach 10.6

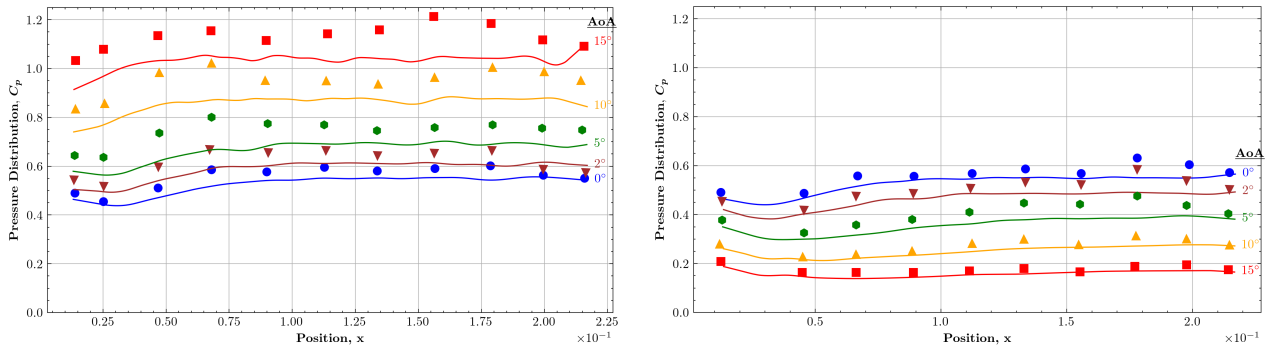

(a) ϕ 0° (b) ϕ 180°

Figure 13 – Model 2 (30° half cone) C_p distribution along the x-axis at Mach 5.25

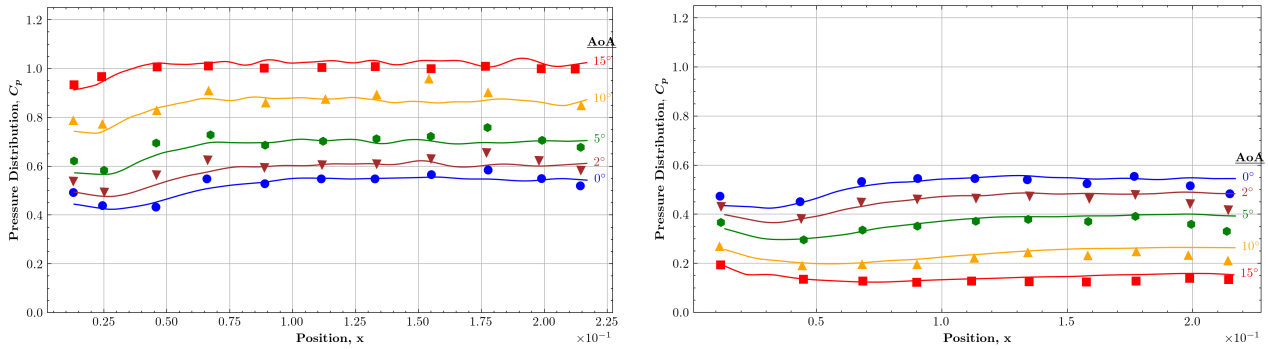

(a) ϕ 0° (b) ϕ 180°

Figure 14 – Model 2 (30° half cone) C_p distribution along the x-axis at Mach 7.4

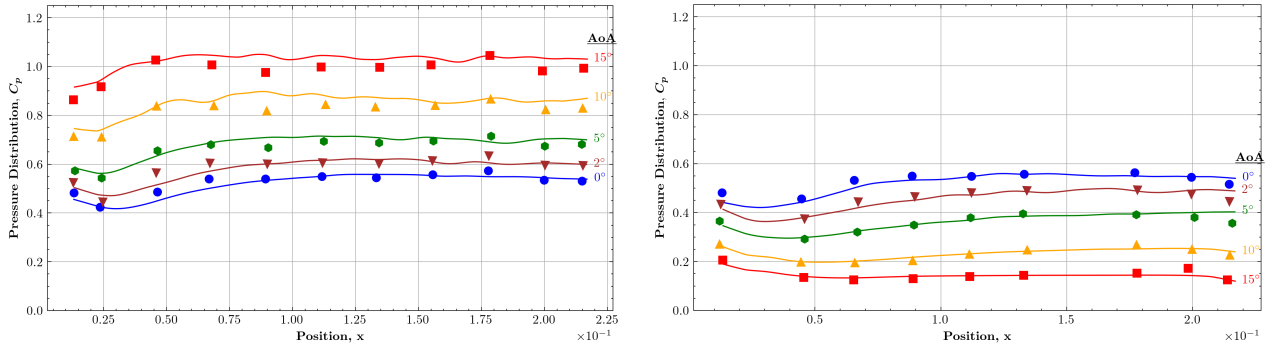

(a) ϕ 0° (b) ϕ 180°

Figure 15 – Model 2 (30° half cone) C_p distribution along the x-axis at Mach 10.6

4.2 Surface Heat Transfer

Heat transfer results were only validated using the Sharp cone test case, since Cleary did not measure any surface heat transfer for the blunted noses in his experiments. Figure 16 presents the comparison of measured and CFD predicted circumferential normalised surface heat transfer rate (h) at the axial measurement plane. This is plotted as the ratio of the local value of h to that at the same location for AoA of zero (h_0).

The circumferential variation of surface heat transfer is similar in shape with that for surface pressure, with the highest values on or close to the windward symmetry line, and a minimum close to the leeward symmetry line. Heat transfer rate is seen to increase with angle of attack on the windward side of the cone.

What is immediately obvious in these comparisons is that, for both turbulence models, the results with real-gas effects modelled far more closely accurately follow the experimental data than those where purely ideal gas is modelled. While the internal gas energetics was found not to be of strong importance in accurately predicting surface pressure, it is of high importance for accurately capturing the heat transfer rate in the highest temperature regions close to the nose apex.

The results also show that Menter's SST version of the k-omega turbulence model is noticeably superior to the Spalart-Allmaras turbulence model in the prediction of the high heat transfer rates at the nose.

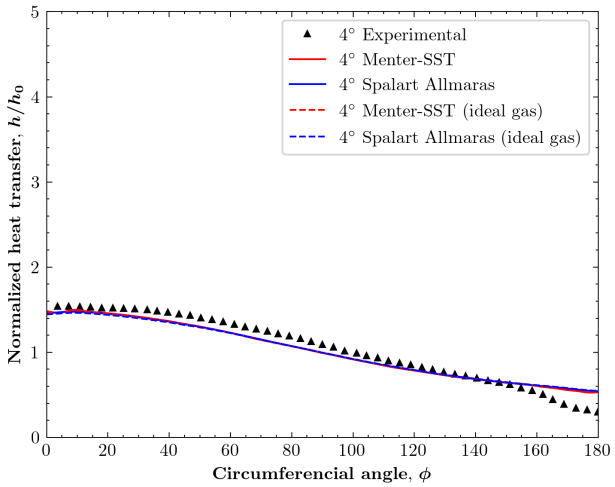

(a) AoA 4°

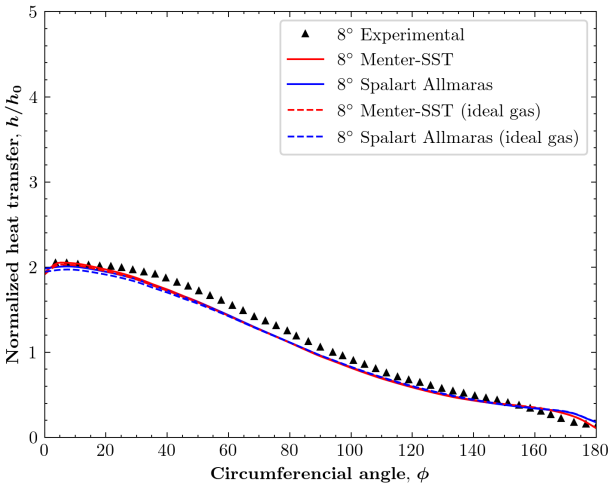

(b) AoA 8°

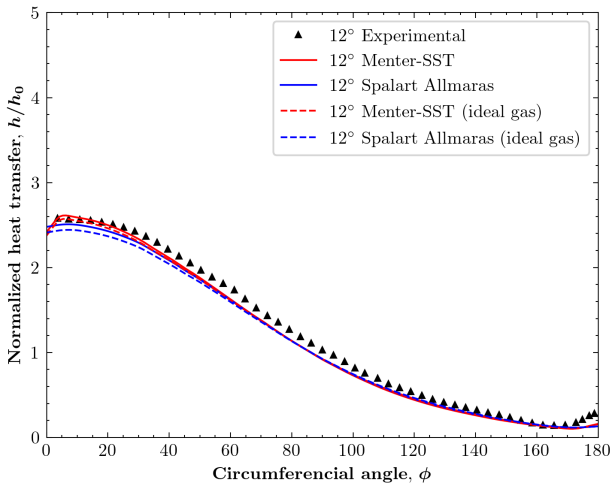

(c) AoA 12°

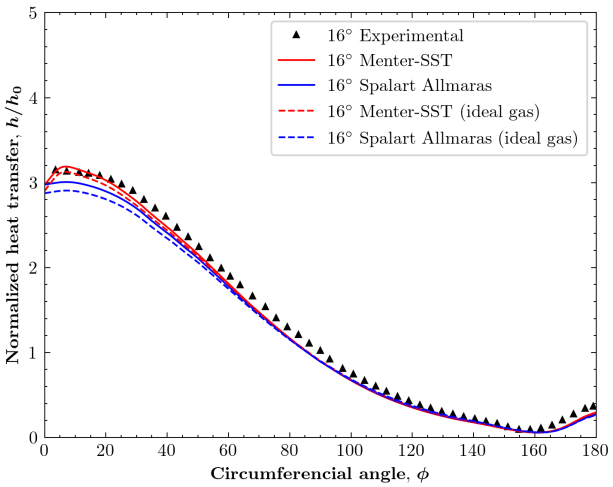

(d) AoA 16°

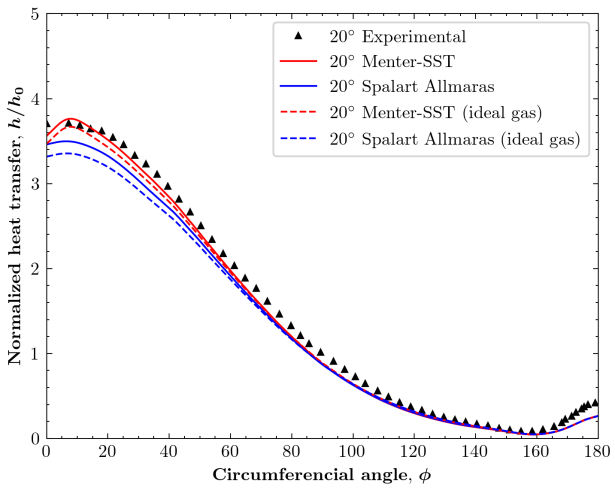

(e) AoA 20°

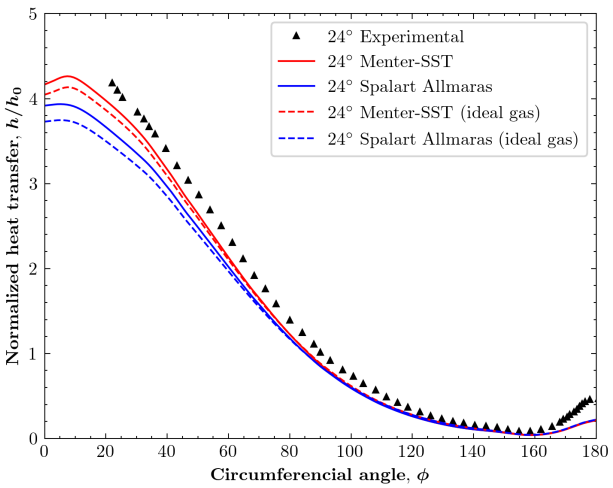

(f) AoA 24°

Figure 16 – Normalised heat transfer along the circumferential axis for the sharp cone case

4.3 The Flowfield

For the Tracey experiment, the crossflow pitot pressure was scanned and the y-z location of the conical shock wave, the boundary layer and separated shear layer and any secondary shock features were captured as the axial measurement station for each angle of attack. Figure 17 presents the comparison of the CFD resolved (in this case for the Menter SST (right) and Spalart-Allmaras(left) model data with real-gas model) crossflow with that identified in the experiment. Here the experimental results follow Tracey's format whereby the different flow features are plotted as lines with specific symbols denoting each feature as follows:

- line + circle: Shockwave
- line + diamond: Viscous Boundary
- line + triangle: Minimum Pitot Pressure
- X: Surface pressure plateau
- The dotted-crossed at the centreline of the figure represents where the cone vertex is located.

The overall trends in the evolution of the crossflow with angle of attack is seen to be captured remarkably well by the CFD method. The position and structure of the bow shock wave is accurately resolved in all cases, although its leeside sharpness dissipates due to reduced mesh resolution. This could be improved using mesh adaption to cluster more cells locally. The viscous CFD method successfully and accurately resolved the thickening of the leeside boundary layer with angle of attack and its separation between $8°$ and $12°$ AoA. It successfully resolves the subsequent development of the separated shear layer at higher angle of attack and the appearance of an embedded separation shock wave and its bifurcation at the highest $24°$ AoA.

The difference between the result from the Menter-SST(right) and Spalart-Allmaras(left) turbulence model was found to be more distinct as incidence angle increases. The contour features captured using the Menter-SST turbulence model were found to be much closer to the experimentally resolved ones than those predicted by the Spalart-Allmaras model.

The flow visualisation for the blunted cone models were achieved using the shadowgraph imaging technique. However, only the $15°$ half cone model at AoA $0°$ and $5°$, at Mach 7.4 have available results in Cleary's paper. A numerical shadowgraph image was generated using custom functions for the corresponding CFD solutions utilising the density gradient to compare with the experimental shadowgraph. The results show very consistent correlation between the experimental and numerical image of the shock wave shape and location as seen in Figure 18.

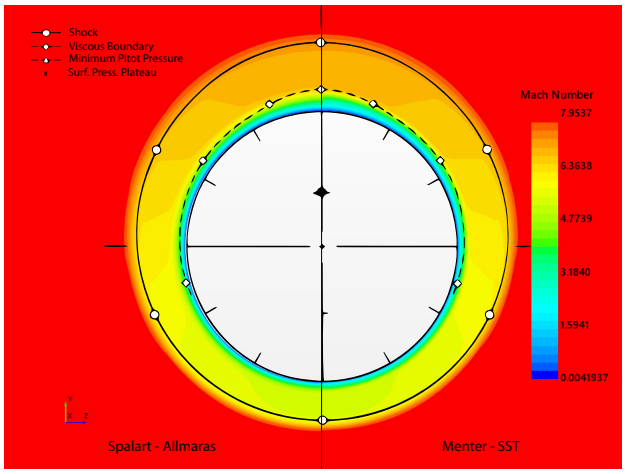

(a) AoA 4°

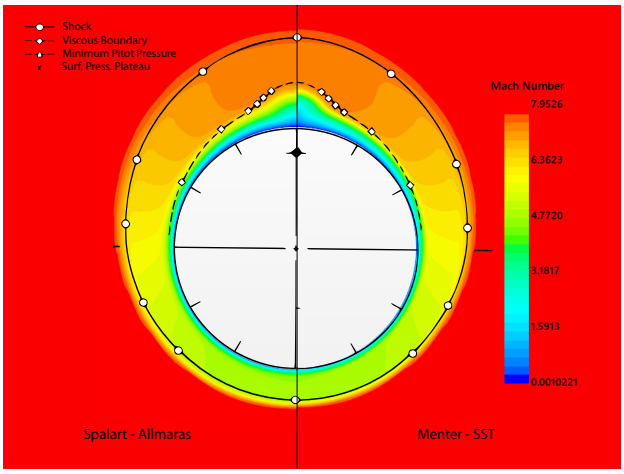

(b) AoA 8°

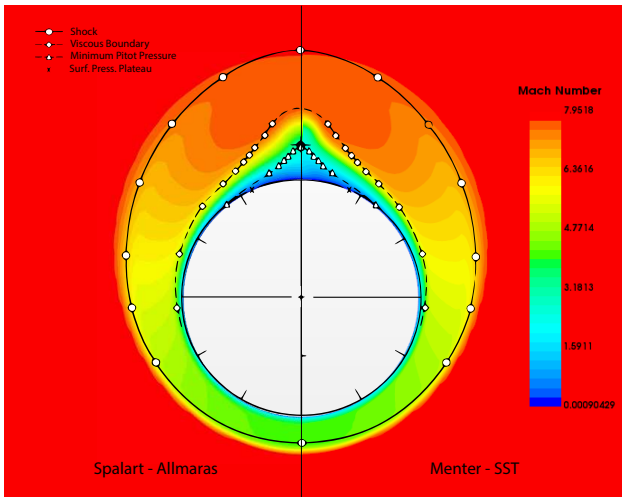

(c) AoA 12°

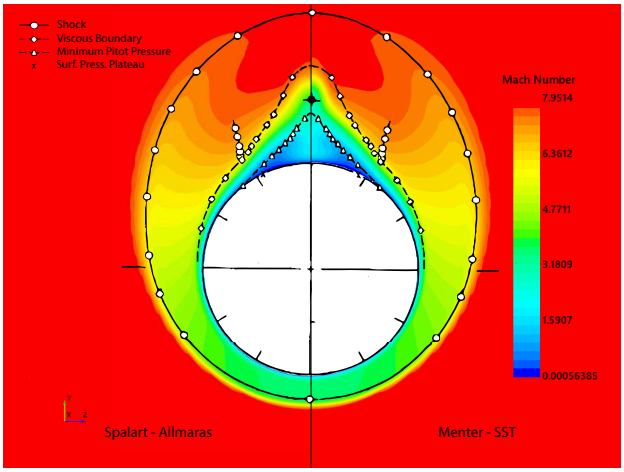

(d) AoA 16°

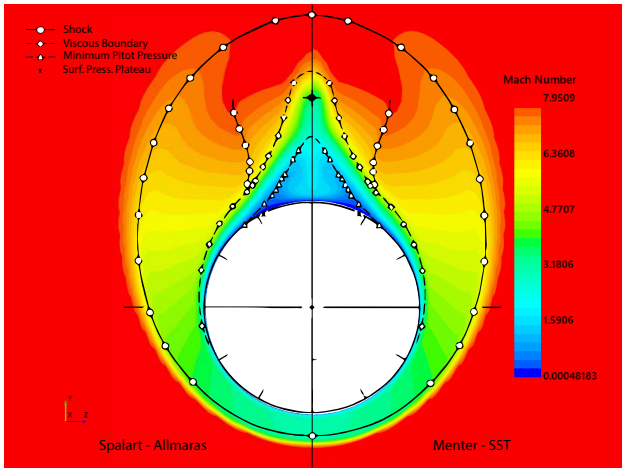

(e) AoA 20°

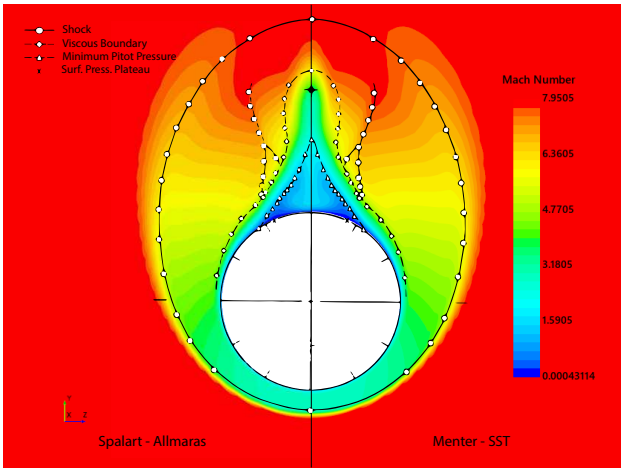

(f) AoA 24°

Figure 17 – Crossflow structure comparisons of the sharp cone at various angles of attack (CFD: Menter SST (left) and Spalart-Allmaras(right) model with real-gas model)

(a) AoA $0°$

(b) AoA $5°$ windward

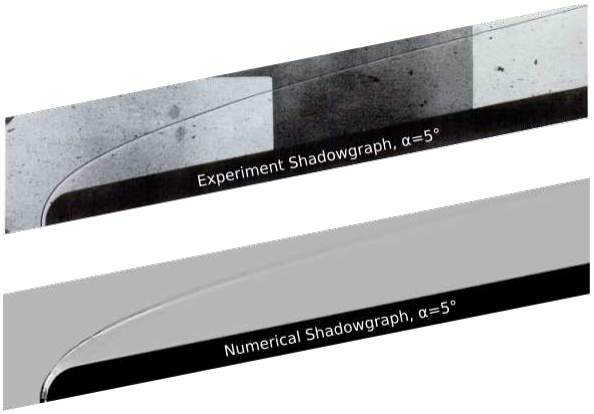

(c) AoA $5°$ leeward

Figure 18 – Comparison of experimental and numerical shadowgraph images on the symmetry planes (CFD: Mentor SST model with real-gas model)

5. Conclusion

The conclusions derived from this study are as follows:

- Modern Navier-Stokes CFD methods are capable of accurately resolving the complex compressible viscous attached and separated flows about sharp and blunted nosed cones at angle of attack to hypersonic flows with molecular vibration and mild chemical dissociation with associated reactions close to the nose.
- Conventional perfect gas models are sufficient to resolve the surface pressure trends of such flows, but accurate heat transfer and shock location / shape capturing requires the real-gas effects to be properly modelled.
- Of those turbulence models tested in this study the Menter Shear-Stress Transport version of the k-Omega turbulence model was found to be superior for application to inclined hypersonic cone flows.
- For follow on studies involving configurations with control surfaces and other features seen on missiles and entry body designs, these correct modelling guidelines for the capture of the flow characteristics around the baseline body will be of some benefit.

6. Copyright Statement

7. Author Contact Information

Einar Karl Tucio Carias
e.carias@cranfield.ac.uk
+447446366845

References

[1] Ambrosio, Alphonso and Wortman, Andrzej. Stagnation-point shock-detachment distance for flow around spheres and cylinders in air. *Journal of the Aerospace Sciences*, 29(7):875–875, 1962.

[2] Bannink, WJ and Nebbeling, C. Measurements of the supersonic flow field past a slender cone at high angles of attack. *AGARD High Angle of Attack Aerodyn. 15 p(SEE N 79-21996 13-01)*, 1979.

[3] Bartlett, Ro S. Tables of supersonic symmetrical flow around right circular cones, with and without the addition of heat at the wave. 1966.

[4] Billig, Frederick S. Shock-wave shapes around spherical-and cylindrical-nosed bodies. *Journal of Spacecraft and Rockets*, 4(6):822–823, 1967.

[5] Cheng, HK. Hypersonic flows past a yawed circular cone and other pointed bodies. *Journal of Fluid Mechanics*, 12(2):169–191, 1962.

[6] Cleary, Joseph W. *An experimental and theoretical investigation of the pressure distribution and flow fields of blunted cones at hypersonic mach number*. National Aeronautics and Space Administration, 1965.

[7] Cross, Peter G. and West, Michael R. Simulation of hypersonic flowfields using star-ccm +. Technical report, Naval Air Warfare Center Weapons Division China Lake United States, 2019.

[8] Deepak, NR; Ray, Taprabata, and Boyce, Russell. Nose cone design optimization for a hypersonic flight experiment trajectory. In *14th AIAA/AHI Space Planes and Hypersonic Systems and Technologies Conference*, page 7998, 2006.

[9] Désidéri, Jean-Antoine; Glowinski, Roland, and Périaux, Jacques. *Hypersonic Flows for Reentry Problems: Volume II: Test Cases—Experiments and Computations Proceedings of a Workshop Held in Antibes, France, 22–25 January 1990*. Springer Science & Business Media, 1991.

[10] Doty, Roberto T and Rasmussen, Maurice L. Approximation for hypersonic flow past an inclined cone. *AIAA Journal*, 11(9):1310–1315, 1973.

[11] Ferri, Antonio. Supersonic flow around circular cones at angles of attack. Technical report, 1951.

[12] Garimella, Rao V; Kim, Jibum, and Berndt, Markus. Polyhedral mesh generation and optimization for non-manifold domains. In *Proceedings of the 22nd International Meshing Roundtable*, pages 313–330. Springer, 2014.

[13] Greenshields, Christopher J; Weller, Henry G; Gasparini, Luca, and Reese, Jason M. Implementation of semi-discrete, non-staggered central schemes in a colocated, polyhedral, finite volume framework, for high-speed viscous flows. *International journal for numerical methods in fluids*, 63(1):1–21, 2010.

[14] Gupta, Roop N.; Lee, Kam-pui; Thompson, Richard A., and Yos, Jerrold M. Calculations and Curve Fits of Thermodynamic and Transport Properties for Equilibrium Air to 30000 K. Technical report, 1991.

[15] Kopal, Zdeněk. *Tables of supersonic flow around cones*. Number 1. Mass. Inst. of Technology, 1947.

[16] Kopal, Zdeněk. *Tables of supersonic flow around yawing cones*. Massachusetts Institute of Technology, 1947.

[17] Lee, Joon and Rho, Oh. Numerical analysis of hypersonic viscous flow around a blunt body using Roe's FDS and AUSM+ schemes. In *28th Fluid Dynamics Conference*, Reston, Virigina, jun 1997. American Institute of Aeronautics and Astronautics. doi: 10.2514/6.1997-2054.

[18] Lee, Joon and Rho, Oh. Accuracy of AUSM+ scheme in hypersonic blunt body flow calculations. In *8th AIAA International Space Planes and Hypersonic Systems and Technologies Conference*, Reston, Virigina, apr 1998. American Institute of Aeronautics and Astronautics. doi: 10.2514/6.1998-1538.

[19] Legendre, R. Lignes de courant dun ecoulement continu. *Recherche Aerospatiale*, (105):3, 1965.

[20] Lighthill, MJ. Supersonic flow past slender bodies of revolution the slope of whose meridian section is discontinuous. *The Quarterly Journal of Mechanics and Applied Mathematics*, 1(1):90–102, 1948.

[21] Maccoll, JW. The conical shock wave formed by a cone moving at a high speed. *Proceedings of the Royal Society of London. Series A-Mathematical and Physical Sciences*, 159(898):459–472, 1937.

[22] Mavriplis, Dimitri J. Unstructured-mesh discretizations and solvers for computational aerodynamics. *AIAA journal*, 46(6):1281–1298, 2008.

[23] Mavriplis, DJ. Unstructured grid techniques. *Annual Review of Fluid Mechanics*, 29(1):473–514, 1997.

[24] Menter, F. Zonal Two Equation k-w Turbulence Models For Aerodynamic Flows. In *23rd Fluid Dynamics, Plasmadynamics, and Lasers Conference*, Reston, Virigina, jul 1993. American Institute of Aeronautics and Astronautics. doi: 10.2514/6.1993-2906.

[25] Menter, F. R. Two-equation eddy-viscosity turbulence models for engineering applications. *AIAA Journal*, 32(8):1598–1605, aug 1994. ISSN 0001-1452. doi: 10.2514/3.12149.

[26] Paull, A; Alesi, H, and Anderson, S. The development of the hyshot flight program. In *Shock Waves*, pages 31–48. Springer, 2005.

[27] Peake, David J and Tobak, Murray. Three-dimensional interactions and vortical flows with emphasis on high speeds. Technical report, Advisory Group For Aerospace Research and Development Neuilly-Sur-Seine (France), 1980.

[28] Rainbird, William John. Turbulent boundary-layer growth and separation on a yawed cone. *AIAA Journal*, 6 (12):2410–2416, 1968.

[29] Rasmussen, Maurice L. On hypersonic flow past an unyawed cone. *AIAA Journal*, 5(8):1495–1497, 1967.

[30] Rom, Josef. *High angle of attack aerodynamics: subsonic, transonic, and supersonic flows*. Springer Science & Business Media, 2012.

[31] Schlichting, Hermann and Gersten, Klaus. *Boundary-Layer Theory*. Springer Berlin Heidelberg, Berlin, Heidelberg, 9th edition, 2017. ISBN 978-3-662-52917-1. doi: 10.1007/978-3-662-52919-5.

[32] Sims, Joseph L. *Tables for supersonic flow around right circular cones at small angle of attack*, volume 3007. Scientific and Tecnical Information Division, National Aeronautics and Space . . . , 1964.

[33] Sobieczky, Helmut. Parametric airfoils and wings. In *Recent development of aerodynamic design methodologies*, pages 71–87. Springer, 1999.

[34] Sommer, Simon C and Stark, James A. The effect of bluntness on the drag of spherical-tipped truncated cones of fineness ratio 3 at mach numbers 1.2 to 7.4. Technical report, 1952.

[35] Spalart, P. and Allmaras, S. A one-equation turbulence model for aerodynamic flows. In *30th Aerospace Sciences Meeting and Exhibit*, Reston, Virigina, jan 1992. American Institute of Aeronautics and Astronautics. doi: 10.2514/6.1992-439.

[36] Stone, AH. On supersonic flow past a slightly yawing cone. *Journal of Mathematics and Physics*, 27(1-4): 67–81, 1948.

[37] Tracey, Richard R. Hypersonic Flow over a Yawed Circular Cone. *Hypersonic Research Project Memorandum*, page 15, 1963.

[38] Tsien, Hsue-Shen. Supersonic flow over an inclined body of revolution. *Journal of the Aeronautical Sciences*, 5(12):480–483, 1938.

[39] Van Dyke, Milton D. A study of hypersonic small disturbance theory. Technical report, 1954.

[40] Versteeg, Henk Kaarle and Malalasekera, Weeratunge. *An introduction to computational fluid dynamics: the finite volume method*. Pearson education, 2007.

[41] Von Karman, Theodore and Moore, Norton B. *Resistance of slender bodies moving with supersonic velocities, with special reference to projectiles*. Guggenheim Aeronautical Laboratory, 1932.

[42] Wallskog, Harvey A and Hart, Roger G. *Investigation of the Drag of Blunt-nosed Bodies of Revolution in Free Flight at Mach Numbers from 0.6 to 2.3*. National Advisory Committee for Aeronautics, 1953.

[43] Ward, LC. Measurements of pressure distributions and pressure drags at zero incidence on both blunt and sharp axisymmetric forebodies. 1976.

[44] Werle, H. Separation on axisymmetrical bodies at low speed. *La Recherche Aeronautique*, 90:3–14, 1962.

[45] Zakkay, Victor; Calarese, Wladimiro, and Wang, C.R. A theoretical and experimental investigation of the hypersonic turbulent boundary layer subject to normal and longitudinal pressure gradients and cross flow along a windward plane of symmetry. In *10th Aerospace Sciences Meeting*, page 187, 1972.